Structure of large-scale vortices and unsteady reverse flow in the reattaching zone of a turbulent separation bubble

By MASARU KIYA and KYURO SASAKI

Faculty of Engineering, Hokkaido University, Sapporo, 060, Japan

This paper describes experiments concerning the structure of large-scale vortices and the unsteady reverse-flow properties in the reattaching zone of a nominally two-dimensional separation bubble formed at the leading edge of a blunt flat plate with right-angled corners. The experiment was performed in a wind tunnel with a constant Reynolds number 2.6×10^4 (based on the main-flow velocity and the thickness of the plate). Split-film probes, being sensitive to instantaneous reversals of flow direction, were extensively employed. An important feature of this study is a judicious use of surface-pressure fluctuations as a conditioning signal to educe the structure of the large-scale vortices.

Distributions of fluctuating-velocity vectors and contour lines of high-frequency turbulent energy in a few space–time domains are presented and discussed. The most economical interpretation of these space–time distributions is that the large-scale vortices in the reattaching zone are hairpin vortices whose configuration is sketched in the text. The unsteady flow in the reattaching zone is mainly governed by two agents; the motion of the large-scale vortices and the low-frequency unsteadiness. The unsteady flow is clarified in terms of the motion (in a space–time domain) of zeros of the longitudinal velocity close to the surface of the plate; the effects of the two agents on this motion are presented separately. On the basis of these results, a mathematical model of the unsteady flow in the reattaching zone is suggested and found to yield good comparison with measured reverse-flow intermittency and frequency of local-flow reversals. It appears that the separation bubble experiences shrinkage and enlargement in connection with the low-frequency unsteadiness and that the speed of shrinkage is much greater than that of enlargement. The strength of the large-scale vortices in the reattaching zone seems to be dependent on the phase of the low-frequency unsteadiness.

1. Introduction

In a preceding paper (Kiya & Sasaki 1983, hereinafter referred to as KS), turbulence structure in a two-dimensional separation bubble formed at the leading edge of a blunt plate with right-angled corners (figure 1) was reported; that is, time-mean and r.m.s. velocities, Reynolds shear stress, power spectra, coherence and phase of velocity and surface-pressure fluctuations, reverse-flow intermittency, integral time- and lengthscales and phase velocities of the fluctuations, etc. A list of related works is given in KS. Moreover, a review of separation bubbles behind backward-facing steps is presented by Eaton & Johnston (1981). The main results of KS relevant to the themes of the present paper can be summarized as follows.
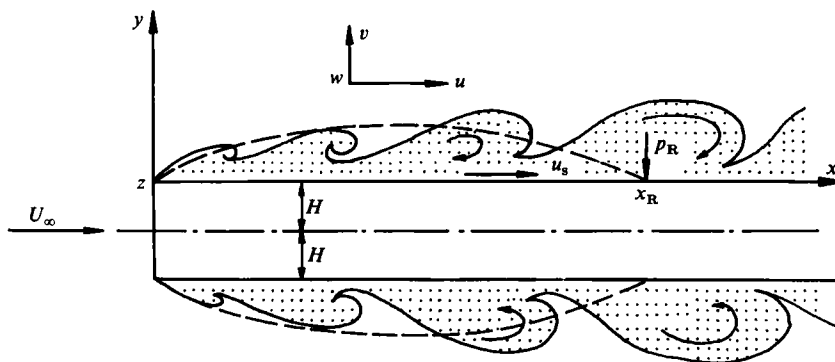
FIGURE 1. Configuration of flow and definition of symbols. Shaded areas are regions with vorticity and broken lines denote time-mean dividing streamlines.

(i) The longitudinal and spanwise integral lengthscales increase linearly with increasing distance x measured from the separation line until the time-mean reattachment line is reached. In the reattaching zone, the longitudinal and spanwise scales are approximately $0.12x_R$ and $0.3x_R$, respectively, x_R being the length of the bubble. The reattaching zone is defined as a region $0.8 \lesssim x/x_R \lesssim 1.2$ where the reverse-flow intermittency is between 0.1 and 0.9. The aspect ratio of large-scale vortices in the reattaching zone is thus 2.5, which shows that the vortices are highly three-dimensional.

(ii) The large-scale vortices are shed downstream from the reattaching zone with a frequency of approximately $0.65U_\infty/x_R$, U_∞ being the free-stream velocity. The average distance between two consecutive large-scale vortices is $(0.7\text{–}0.8)$ x_R in the reattaching zone. These features are also reported by Hillier & Cherry (1981). The effective centre of the vortices is located approximately at $0.2x_R$ above the plate surface.

(iii) There exists a large-scale, low-frequency unsteadiness in the separation bubble whose frequency is less than $0.25U_\infty/x_R$; the central frequency is $0.12U_\infty/x_R$, which is approximately one-sixth of the vortex-shedding frequency. In what follows, this unsteadiness will be called the low-frequency unsteadiness. This is also observed in the same separation bubble by Hillier & Cherry (1981) and Cherry, Hillier & Latour (1984) and in the separation bubble behind a backward-facing step by Eaton & Johnston (1982).

(iv) A pair of counter-rotating streamwise (or longitudinal) vortices probably exists in the reattaching zone. The spanwise distance between the streamwise vortices is approximately $0.6x_R$. A flow-visualization study suggests that they are ends of a hairpin vortex.

In the present paper, the structure of the large-scale vortices and the unsteady reverse flow in the reattaching zone will be clarified in more detail than in KS by means of conditional-sampling techniques.

The flow in the reattaching zone is of practical importance because the heat- and mass-transfer rates and the r.m.s. surface pressure attain a maximum near the time-mean reattachment line, which is the middle of the reattaching zone (Hillier & Cherry 1981; Ota & Kon 1974, among others). The structure of turbulence in this zone, however, it not well understood yet (Eaton & Johnston 1981), and hence has been a subject of several experimental studies (Bradshaw & Wong 1972; Chandrsuda & Bradshaw 1981; Wood & Bradshaw 1982). These studies are mostly concerned with

measurements of Reynolds stresses, turbulence intermittency, power spectra, single- and two-point correlations of velocity fluctuations, and discussions of the turbulent-energy balance. In this paper, a different approach is employed; that is, space–time distributions of fluctuating velocity vectors in the large-scale vortices are obtained to demonstrate their structure; the unsteady reverse-flow property in the reattaching zone is discussed in terms of the motion of the large-scale vortices and the low-frequency unsteadiness. These are effected by conditional-sampling techniques employing the surface-pressure fluctuations as a conditioning signal.

The configuration of the flow and definition of symbols are illustrated in figure 1. The Cartesian coordinates x, y, z are defined in such a way that the x-axis is in the longitudinal direction along a side, the y-axis is normal to the side and the z-axis is along one of the separation edges normal to the x- and y-axes so as to form a right-handed system. The thickness of the plate is denoted by $2H$. The velocity components in the x-, y- and z-directions and the surface pressure are denoted by u, v, w and p, respectively, and the corresponding fluctuating components by u', v', w' and p'. The velocity at infinity upstream is denoted by U_∞. The distance from the separation edge to the time-mean reattachment line is written as x_R.

2. Experimental apparatus and methods

The experimental apparatus was almost the same as that employed in KS, and so only a brief description will be given. The thickness $2H$ of the plate tested was 20 mm and its aspect ratio was 10. The distance between the leading edge and the time-mean reattachment line x_R was $10.1H$. The somewhat small span may be responsible for some of observed three-dimensional features which will be presented in §3.1. This point will be discussed later. The measurements were made at a constant Reynolds number $U_\infty(2H)/\nu = 2.6 \times 10^4$, ν being the kinematic viscosity. The approaching-flow velocity was slightly varied in order to maintain a constant Reynolds number but was approximately 20 m/s.

Measurements of the time-mean and fluctuating velocities were made by linearized constant-temperature hot-wire anemometers using single and X-wire probes and split-film probes. The pressure fluctuations on the surface of the plate were detected at the midspan by a semi-conductor strain-gauged transducer mounted inside the test plate with a small cavity between the pressure tap and the diaphragm of the transducer. The hot-wire probes, the split-film probes and the pressure transducer were operated and calibrated as described in KS. The maximum frequency of response was approximately 10 and 1.5 kHz for the hot wires and the split films, respectively. The gain factor of the pressure transducer was 1 ± 0.06 up to 530 Hz with a negligibly small phase shift.

A static-pressure probe shown in figure 2 was used, together with the built-in pressure transducer, to measure cross correlations of pressure fluctuations at two points on and near the surface. This is a thin round tube 1.3 mm in diameter, bent into an L-shape at a position 7 mm from one end; the other end was closed by solder and shaped into a hemispherical form. Four pressure taps 0.5 mm in diameter were drilled onto the tube at a position 9 mm from the hemispherical edge; the other end was directly connected to a semi-conductor strain-gauged pressure transducer (Toyoda P104K) to form a static-pressure probe.

The response of this probe to fluctuating static pressures was examined as follows. First we measured with this probe the longitudinal distribution of the r.m.s. value of the pressure fluctuations (in the separation bubble) at a height 1 mm above the
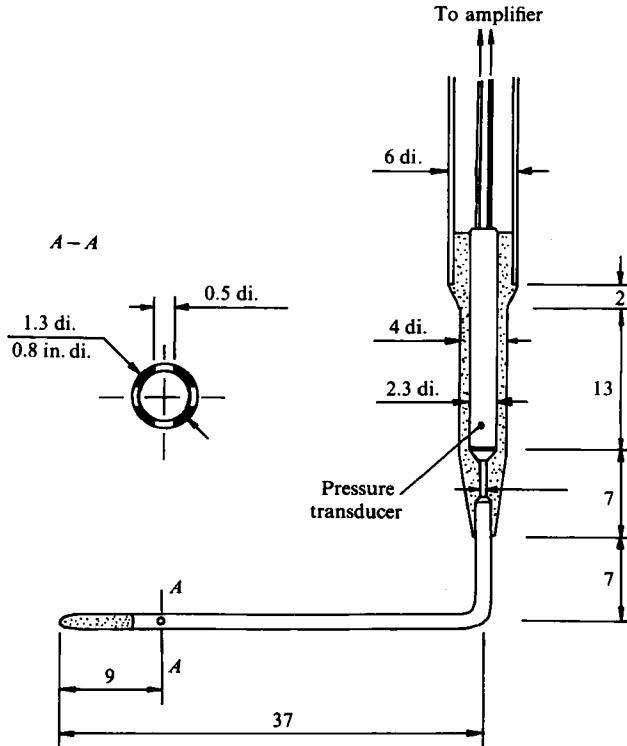
FIGURE 2. Probe for measurement of fluctuating static pressure near solid surface. Dimensions in mm.

surface. The result was in good agreement with that obtained by a built-in transducer within the separation bubble. Secondly, the probe was again set at the same height to measure the longitudinal and spanwise correlations between its output and the output of the built-in transducer fixed at the mid-span of the time-mean reattachment line. The results agreed well with those of Cherry *et al.* (1984) (figures 10 and 33 of their paper). Accordingly the probe may be used to measure approximately the surface-pressure fluctuations.

The velocity and pressure fluctuations were recorded on two or three channels of an analog tape recorder over a sample time 10.44 s and later digitized and analysed by a computer (HITAC M200H). Some of the analogue data were analysed by a digital signal processor (SANEI 7T07A). The sample time was sufficiently long to provide stationary averages because it was approximately 1400 times the period of shedding of large-scale vortices from the reattaching zone.

The intermittency function of turbulence $i_T(t)$, t being time, is defined as unity for turbulent regions and as zero for non-turbulent regions. As described in KS, this was obtained in terms of the square of the high-pass-filtered longitudinal velocity fluctuation u'_T. The cut-off frequency was chosen as 4 kHz because the dissipation spectrum of u' attains a maximum at this frequency. The high-frequency fluctuation u'_T has such small amplitude that u'^2_T is not influenced markedly in character by reversals of the local flow direction. Accordingly, u'_T was detected by a single hot-wire probe.

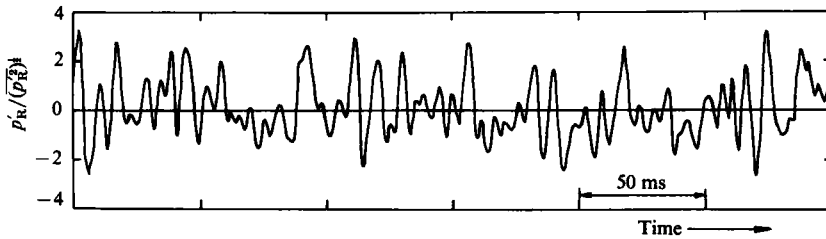In the same way, the intermittency function of reverse flow $i_r(t)$ is defined as unity

FIGURE 3. An example of waveform of surface-pressure fluctuation at time-mean
reattachment point. The waveform is low-pass filtered (550 Hz).

for reverse flows and as zero for forward flows. This function was obtained in terms
of the short-time average of the longitudinal velocity at a height 0.5 mm ($\simeq 0.005x_R$)
from the surface (see KS).

Conditional-sampling measurements of velocity fields associated with the large-scale
vortices and with the low-frequency unsteadiness were made by employing the
surface-pressure fluctuations in the separation bubble as a conditioning signal. As
shown in KS, among others, the surface-pressure fluctuations are strongly correlated
with the motion of the large-scale vortices and the low-frequency unsteadiness. For
example, the pressure fluctuation at a given point in the reattaching zone attains a
valley when a large-scale vortex exists above the point under consideration.

We consider the surface-pressure fluctuation p'_R at the reattachment point.† This
waveform shows valleys and peaks with widely distributed depths and heights. An
example of the waveforms is given in figure 3. The valleys and peaks are an indication
of the three-dimensionality of the large-scale vortices (such as shown in figure 8); that
is, at Reynolds numbers of the order of 10^4 as in this experiment, the spanwise
location of the effective centre of the large-scale vortices passing the position of the
pressure transducer is conjectured to change fairly randomly from one vortex to
another. The spanwise fluctuation of the vortices was observed by a flow visualization
at a Reynolds number of 630; a flow pattern is presented in figure 32 of KS. Thus,
the depth of the valleys is probably a measure of the spanwise distance between the
effective centre of the vortices and the location of the pressure transducer; the smaller
the distance, the deeper is the depth.

The above consideration led to the idea that we can obtain vector fields of the
fluctuating velocities by conditionally averaging the velocities with respect to the
time when the valleys deeper (or the peaks higher) than a threshold level are detected.

In order to find such a valley or a peak, each three successive digitized data were
compared. Prior to this procedure, the conditioning signal p'_R was low-pass filtered
with a cut-off frequency of 550 Hz. This pretreatment was necessary because the
built-in pressure transducer had poor response beyond about 550 Hz and because
high-frequency components of the signals behave as noise in the scheme of detection
of the peaks and valleys mentioned above. The cut-off frequency was approximately
four times the vortex-shedding frequency ($\simeq 130$ Hz).

When properties of the low-frequency unsteadiness were studied, the conditioning
signals were digitally low-pass filtered with a cut-off frequency 50 Hz ($\simeq 0.25U_\infty/x_R$)
which is approximately the highest frequency of the low-frequency unsteadiness. In
what follows, any fluctuation low-pass or high-pass filtered with this cut-off frequency
will be denoted by the suffixes l or h, respectively.

† The reattachment point implies the mid span of the time-mean reattachment line.

The threshold level to define the valleys and peaks of the conditioning signals was chosen by examining a number of their waveforms and the frequency of detection of the valleys and the peaks. The threshold level and the detection frequency will be given in the captions of figures where results are presented.

Finally, it may be noted that the probes traversing in the shear layer and the recirculating zone possibly change the structure of the bubble such as the reattachment length x_R. We did not study this interference in detail but the following features are worth mentioning. When the split-film probes were traversed into the bubble, the r.m.s. surface pressure in the reattaching zone increased by only 1.2% of the undisturbed value. At the same time, the conditioning signal (i.e. the pressure fluctuation at the time-mean reattachment point), which served to construct velocity-vector fields of figures 4–7, yielded a 3.5% smaller number of events satisfying the condition of sampling than in the undisturbed case. Thus we assume that the interference had only a small influence on the structure obtained in the present study.

3. Results and discussion

3.1. *Velocity fields associated with large-scale vortices in the reattaching zone*

The conditionally averaged velocity fluctuations $(\langle u' \rangle, \langle v' \rangle)$ are shown in figures 4 and 5 in the space-time domain (y, t) for the valleys and the peaks of the surface-pressure fluctuation at the reattachment point. Here $\langle \ \rangle$ means the ensemble average. The abscissa is $-U_c t/x_R$, where $U_c (= 0.5U_\infty)$ is the average convection velocity of the large-scale vortices in the reattaching zone (see KS), so that $-U_c t$ can be interpreted as $x - x_R$, viz the longitudinal distance relative to the reattachment point. Figures 4(a) and 5(a) show contour lines† of the high-frequency turbulent energy $\langle u_T'^2 \rangle$ in the same space–time domain. Since u_T' is the fluctuation at frequencies of the order of the Kolmogorov frequency, we assume that a region where $\langle u_T'^2 \rangle$ attains a maximum can be interpreted as a region of large vorticity, viz the central part of a large-scale vortex. We feel this assumption reasonable although it is difficult to give more rigorous justification. Difficulty in measuring the fluctuating vorticity has led us to the employment of $u_T'^2$ as a measure of the vorticity fluctuation.

When the pressure fluctuation p_R' attains a valley of sufficient depth, a large system of flow rotating in the clockwise sense is seen to exist (figure 4b). Since the contour lines of $\langle u_T'^2 \rangle$ show a maximum near the centre of the rotating system, this can be interpreted as a real vortex. The effective centre of the vortex seems to be located at $y/x_R \simeq 0.18$.

On the other hand, when p_R' attains a peak, the vector field $(\langle u' \rangle, \langle v' \rangle)$ (figure 5b) suggests a system rotating in the counterclockwise sense. Although one may imagine this system to be a vortex, it is not an actual vortex in the sense that the high-frequency energy $\langle u_T'^2 \rangle$ at the apparent centre of the rotation is low and separated by maxima on each side of the centre. Thus, we interpret this rotating system as being induced by the large-scale vortices (whose centres are at the maxima of $\langle u_T'^2 \rangle$) so as to satisfy the requirement of continuity. The distance between the maxima is roughly $0.6x_R$. This is not far from the longitudinal distance $(0.7–0.8)x_R$ between two consecutive large-scale vortices in the reattaching zone (KS). This difference is probably caused by an increase in dispersion of the vortices with time departing from the origin $t = 0$. Hillier & Cherry (1981) obtain approximately the same distance $0.65x_R$.

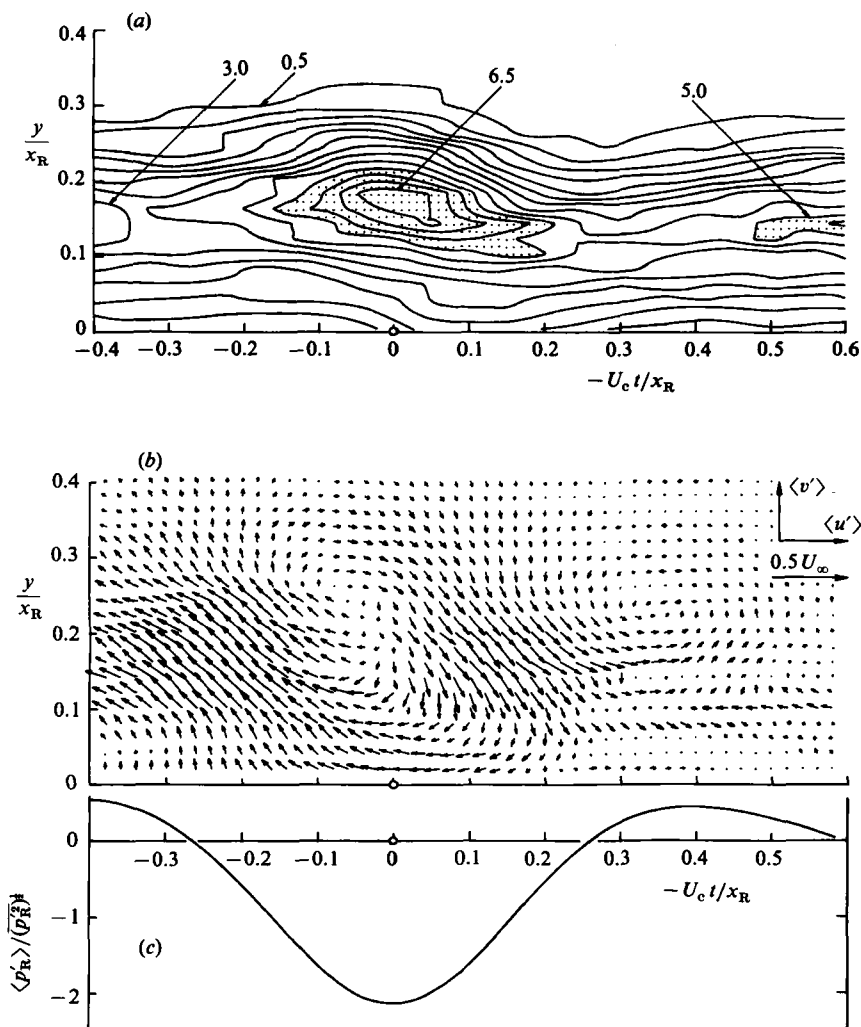† A contour line is defined in this paper as a line on which a quantity is constant.

FIGURE 4. Space–time (y, t) distributions of (a) contour lines of high-frequency turbulent energy $\langle u_T'^2 \rangle$ in a normalized form $10^4 \langle u_T'^2 \rangle / U_\infty^2$ (contour interval 0.5), shaded areas being areas where the normalized energy is higher than 0.5, (b) fluctuating velocity vector $(\langle u' \rangle, \langle v' \rangle)$ and (c) surface-pressure fluctuation at the reattachment point $\langle p_R' \rangle$. Time t is synchronized with valleys of p_R'. Measurements were made in the mid-span plane. The threshold level for the valleys was $-1.8(\overline{p_R'^2})^{\frac{1}{2}}$ and its detection frequency was 43 Hz which is approximately $\frac{1}{3}$ times the vortex-shedding frequency.

We observe in figures 4 (b) and 5 (b) that on the upstream side of the vortex there exists a strong outflow from the wall towards the main stream, while on the downstream side of the vortex an inflow from the main stream takes place. The inflow is expected to transport irrotational fluid of high total energy towards the wall and thus to produce a positive pressure fluctuation of large amplitude at the reattachment point.

Three-dimensional aspects of the large-scale vortices can be obtained from the space-time (z, t) distribution of the conditionally averaged longitudinal and spanwise velocity components $(\langle u' \rangle, \langle w' \rangle)$ and the high-frequency turbulent energy. Results
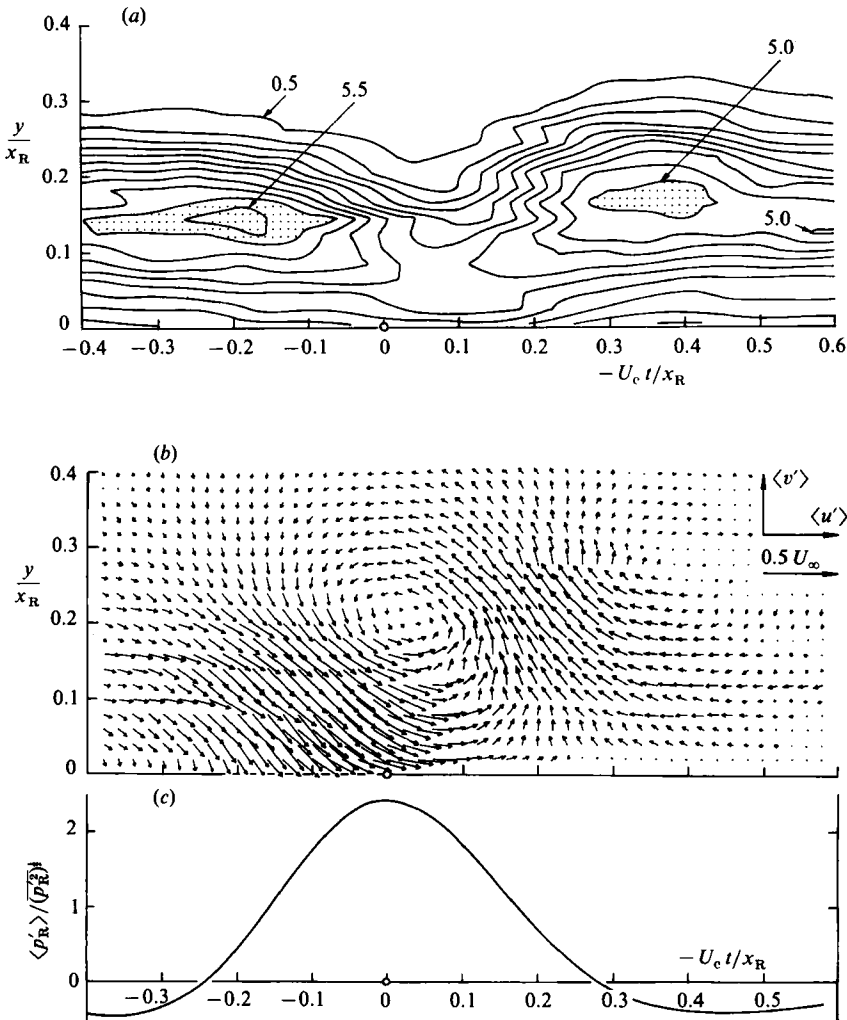
FIGURE 5. Space–time (y, t) distributions of (a) contour lines of high-frequency turbulent energy $\langle u_T'^2 \rangle$ in a normalized form $10^4 \langle u_T'^2 \rangle / U_\infty^2$ (contour interval 0.5), shaded areas being areas where the normalized energy is higher than 0.5, (b) fluctuating velocity vector $(\langle u' \rangle, \langle v' \rangle)$ and (c) surface-pressure fluctuation at the reattachment point $\langle p_R' \rangle$. Time t is synchronized with peaks of p_R'. Measurements were made in the mid-span plane. The threshold level for the peaks was $1.8(\overline{p_R'^2})^{\frac{1}{2}}$ and its detection frequency was 50 Hz which is approximately equal to $\frac{1}{2}$ the vortex-shedding frequency.

are presented in figures 6 and 7 at two heights for the valleys and the peaks. These heights $y/x_R = 0.16$ and 0.32 approximately correspond to the centre y_c and edge y_δ of the shear layer above the reattachment point (KS). For the valleys at the height $y/x_R = 0.16$ (figure 6b), we observe a centre rotating in the clockwise sense at $(-U_c t, -z)/x_R \simeq (-0.1, 0.28)$ and another centre rotating in the clockwise sense approximately at $(0.25, 0.28)$. Contour lines of the high-frequency energy $\langle u_T'^2 \rangle$ show a maximum approximately at the first centre. From the symmetry we expect an image centre at $(-0.1, -0.28)$ corresponding to the first centre. Accordingly, the original and image centres probably indicate a pair of counter-rotating vortices. For
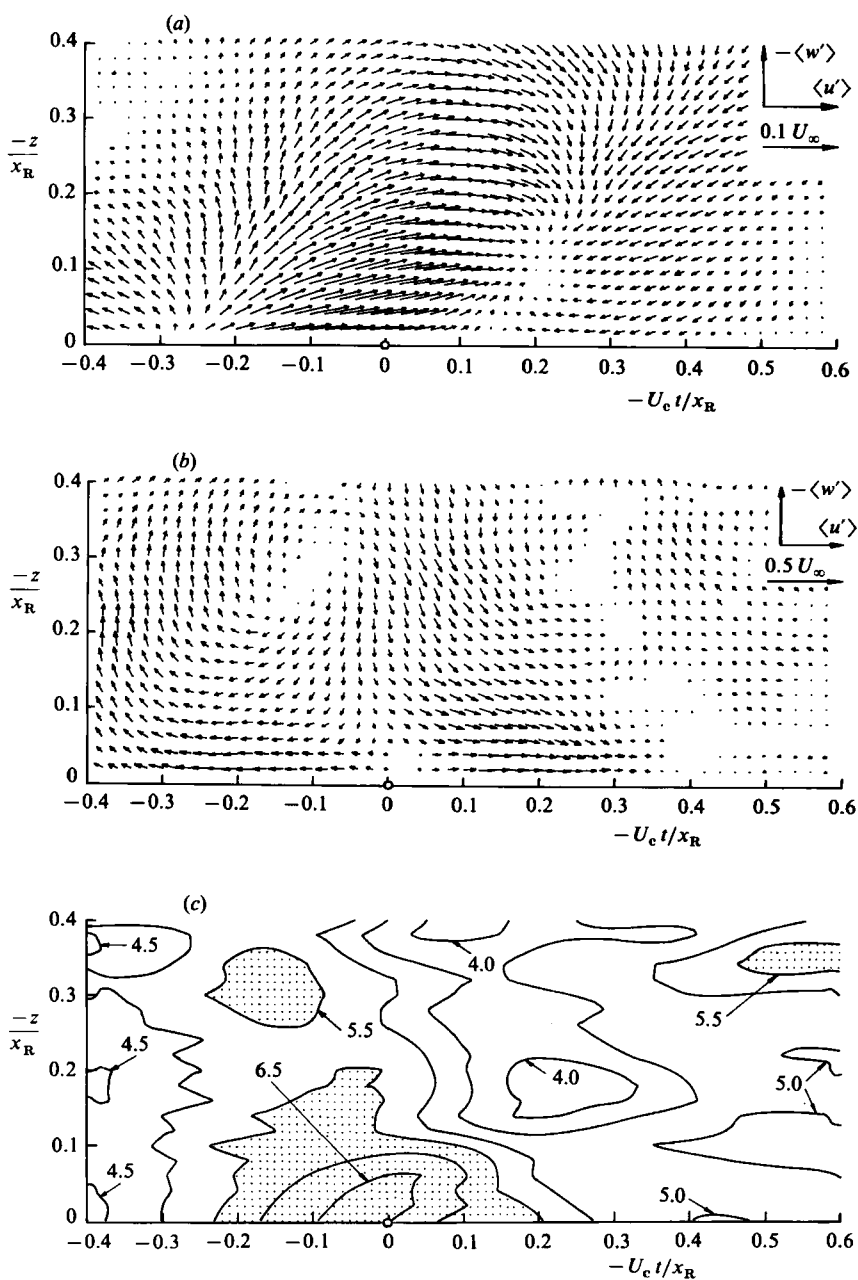
FIGURE 6. Space–time (z, t) distributions of fluctuating velocity vector $(\langle u' \rangle, \langle w' \rangle)$ at height (a) $y/x_{\mathrm{R}} = 0.32$ and (b) 0.16 and (c) contour lines of high-frequency energy $\langle u_{\mathrm{T}}'^2 \rangle$ in a normalized form $10^4 \langle u_{\mathrm{T}}'^2 \rangle / U_\infty^2$ (contour interval 0.5), shaded areas being areas where the normalized energy is higher than 5.5. Time t is synchronized with valleys of p_{R}'.
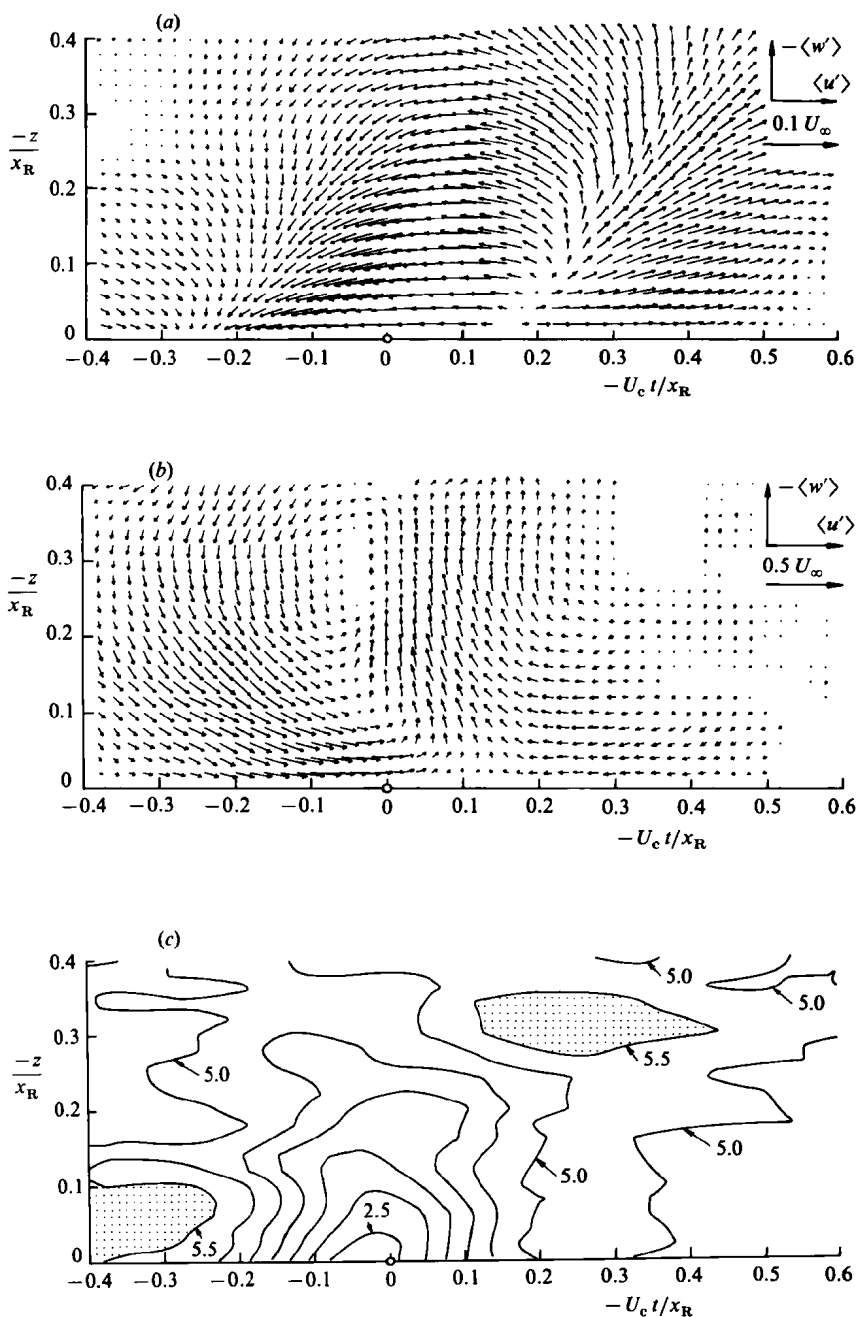
FIGURE 7. Space–time (z, t) distributions of fluctuating velocity vector $(\langle u' \rangle, \langle w' \rangle)$ at height (a) $y/x_R = 0.32$ and (b) 0.16 and (c) contour lines of high-frequency energy $\langle u_T'^2 \rangle$ in a normalized form $10^4 \langle u_T'^2 \rangle / U_\infty^2$ (contour interval 0.5), shaded areas being areas where the normalized energy is higher than 5.5. Time t is synchronized with peaks of p_R'.
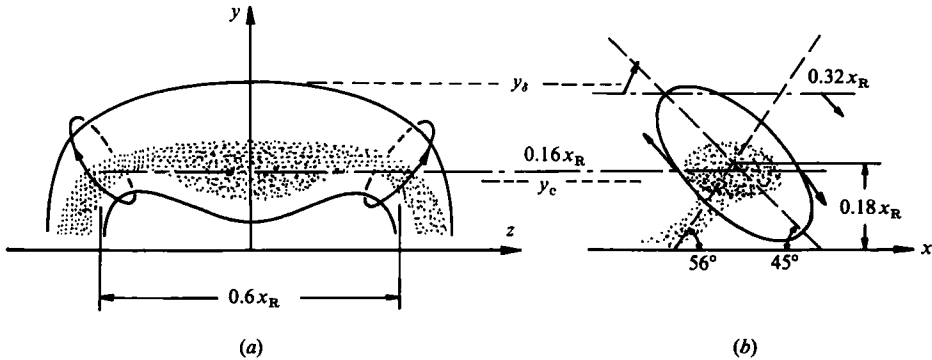
FIGURE 8. A schematic representation of large-scale vortices in the reattaching zone: (a) structure in the (y, z)-plane viewed from the upstream side; (b) section in the (x, y)-plane; dotted areas show core region of the vortex where vorticity is non-zero; the inclined ellipse in (b) is a typical streamline associated with the vortex, see KS.

the valleys at the height $y/x_R = 0.32$ (figure 6a), the vector field suggests a sink-like point at $(-U_c t, -z)/x_R \simeq (-0.25, 0)$ and a source-like point at $(0.2, 0.1)$. It should be noted that the above point-vortex model is strictly a qualitative one used to aid interpretation of the flow field.

The most economical interpretation of the space–time vector fields of figures 4–7, although it may not be the only one, is that the large-scale vortices are hairpin vortices as depicted in figure 8. In constructing figure 8, the results of KS have been considered; the ends of the hairpin vortices have an average inclination of about 56° with respect to the longitudinal direction; the major axis of streamlines of the vortices in the mid-span plane makes an angle of 45° with the longitudinal direction.

Since the span of the separation bubble was only two times its length, the structures of figures 6 and 7 are possibly affected by this somewhat small aspect ratio. We feel, however, that the hairpin vortices depicted in figure 8 are basically the same as those for separation bubbles with higher aspect ratios, although detailed features of the vortices such as the spanwise distance between the ends, the distance between the centres of the vortices and the surface, etc. are perhaps different.

The velocity fields for the peaks (figure 7) have features similar to those for the valleys (figure 6) except for the important difference that the direction of the vectors is exactly opposite: there is a counter-clockwise centre at $(-U_c t, -z)/x_R \simeq (-0.05, 0.28)$ and a clockwise centre very roughly at $(-0.35, 0.3)$ (figure 7b, at the height $y/x_R = 0.16$); a sink-like point at $(-0.25, 0)$ and a source-like point at $(0.2, 0.05)$ (figure 7a, at the height $y/x_R = 0.32$). Moreover, there should be image centres on the side $-z < 0$, corresponding to the clockwise and counter-clockwise centres. Since the contour lines of the high-frequency energy $\langle u_T'^2 \rangle$ show no significant maxima at the counter-clockwise centre, this centre cannot be regarded as an end of the hairpin vortices. Accordingly, we interpret the vector fields of figure 7 for the peaks as being induced between two consecutive hairpin vortices illustrated in figure 8 in order to satisfy the requirement of continuity.

Figure 32 of KS shows that hairpin-like vortices are shed from the reattaching zone, being grouped along the spanwise direction; this observation was made at a Reynolds number of 630. From this and the preceding results, we believe that the pressure fluctuation at a given point in the reattaching zone attains a deep valley when the effective spanwise centre of a hairpin vortex (which is one of the vortices
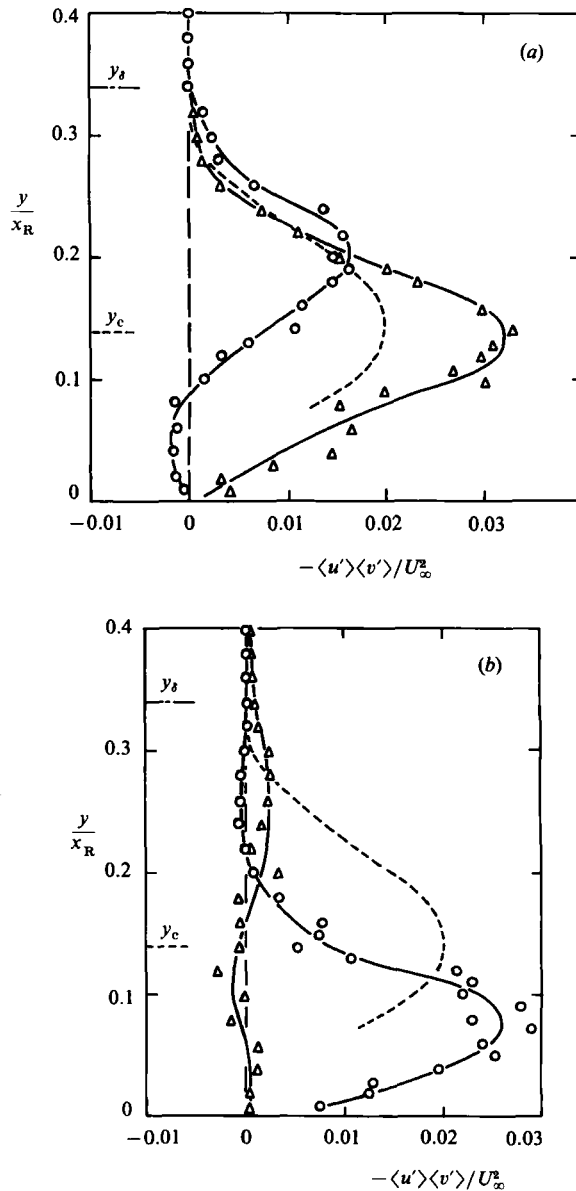
FIGURE 9. Distribution of product $\langle u' \rangle \langle v' \rangle$ in the reattachment section $x/x_R = 1.0$: —––, global Reynolds shear stress $-u'v'/U_\infty^2$; (a) velocity correlation at the time of peaks ($\bigcirc$) and valleys ($\triangle$) of p_R'; (b) velocity product at the time of peaks ($\bigcirc$) and valleys ($\triangle$) of dp_R'/dt. Threshold levels for p_R' and dp_R'/dt were the same, see captions of figures 4 and 5. The frequency of detection of the peaks and valleys of dp_R'/dt was 82 Hz and 110 Hz, respectively.

grouped in the spanwise direction) is above the point under consideration. On the other hand, the pressure fluctuation attains a high peak when that point is midway between two consecutive groups of the vortices.

The dynamical significance of the large-scale vortices in the reattaching zone can be demonstrated by the product $-\langle u' \rangle \langle v' \rangle$ because this gives the extent to which the velocity fluctuations associated with such vortices contribute to the overall
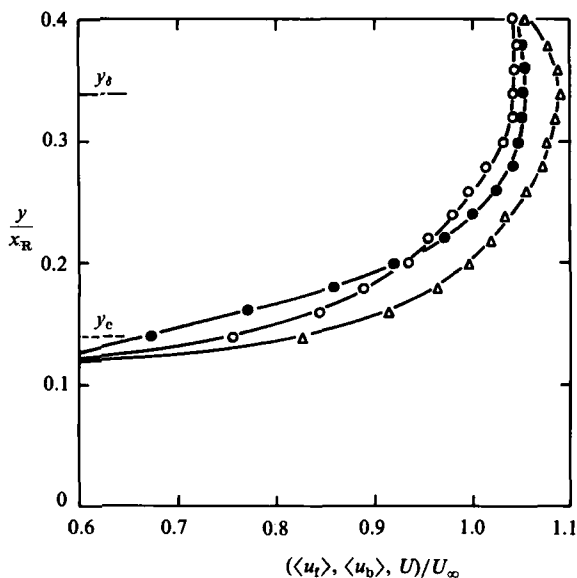
FIGURE 10. Distribution of longitudinal velocity $\langle u_f \rangle$ and $\langle u_b \rangle$ of the front and back, respectively, of large-scale vortices measured in the reattachment section $x/x_R = 1.0$: $\triangle$, $\langle u_f \rangle$; $\bigcirc$, $\langle u_b \rangle$; $\bullet$, time-mean velocity U.

Reynolds shear stress. Figure 9 shows this product at the times when the peaks or valleys of p'_R and its time derivative $\mathrm{d}p'_R/\mathrm{d}t$ were detected. It should be noted that a peak of $\mathrm{d}p'_R/\mathrm{d}t$ appears approximately at a time midway between a valley and a following peak of p'_R and that a valley of $\mathrm{d}p'_R/\mathrm{d}t$ appears between a peak and a following valley of p'_R. In other words, the peaks and the valleys of $\mathrm{d}p'_R/\mathrm{d}t$ appear roughly near the back edge and the front edge, respectively, of the large-scale vortices. Here the front edge of a vortex is the edge first approaching a stationary observer when the vortex translates, whereas the back edge is the edge next approaching the observer.

Figure 9 demonstrates that a large Reynolds shear stress is produced near the front and back edges of the large-scale vortices and midway between two consecutive vortices. Since the fluctuating velocity vector $(\langle u' \rangle, \langle v' \rangle)$ is mostly parallel or normal to the longitudinal direction in the central part of the large-scale vortices (figure 4b), very little Reynolds shear stress is produced there, as shown in figure 9(a). Accordingly, the large-scale vortices are the most dominant feature of turbulence in the reattaching zone.

3.2. *Further aspects of large-scale vortices*

Properties of the high-frequency turbulent energy u'^2_T in the reattaching zone can show further aspects of the large-scale vortices. The front and back of a large-scale vortex were assumed to be detected when the intermittency function of turbulence $i_T(t)$ changes from zero to unity and from unity to zero, respectively. The longitudinal velocity u was averaged at the front and back of a large number of the large-scale vortices; the averaged velocity of the front is denoted by $\langle u_f \rangle$ and that of the back by $\langle u_b \rangle$. The result is presented in figure 10, which shows that the front moves faster than the back by approximately $0.05U_\infty$. Thus, the longitudinal extent of the large-scale vortices increases downstream. On the other hand, as shown in KS, the
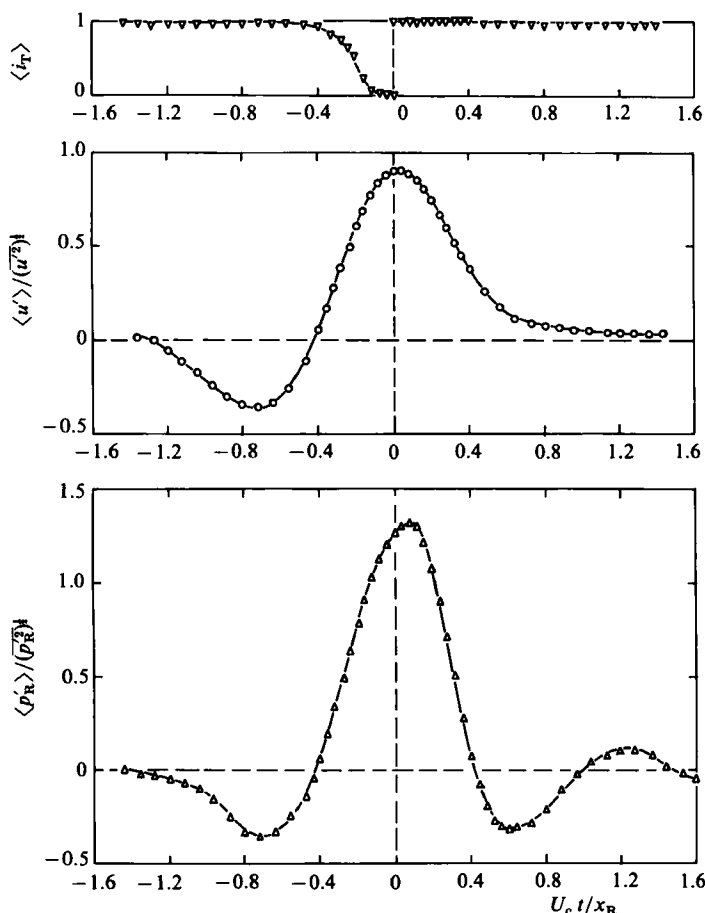
FIGURE 11. Conditionally averaged waveforms of turbulence probability $\langle i_{\mathrm{T}} \rangle$, longitudinal velocity fluctuation $\langle u' \rangle$ and surface-pressure fluctuation $\langle p'_{\mathrm{R}} \rangle$ in the reattachment section: i_{T} and u' were detected at the centre y_{c} of the shear layer; time t is synchronized with the time at which i_{T} changes from zero to unity.

longitudinal integral lengthscale of the large-scale vortices is fairly constant in the reattaching zone. This seemingly contradictory result can be understood if one recalls that an increase in the turbulent region of a large-scale vortex does not necessarily lead to an increase in the well-correlated region of the vortex. What really happens is probably that the poorly correlated part of the vortices is increasing downstream, while the extent of the well-correlated central part remains fairly constant. This is a mechanism of diffusion of vorticity in the large-scale vortices.

Figure 11 shows the conditionally averaged waveforms of the longitudinal-velocity and surface-pressure fluctuations ($\langle u' \rangle$ and $\langle p'_{\mathrm{R}} \rangle$) at the centre of the shear layer above the reattachment point; the synchronization time was chosen as the time when the turbulence intermittency function $i_{\mathrm{T}}(t)$ increases from zero to unity. The conditional averaging of the intermittency function $\langle i_{\mathrm{T}} \rangle$ is also included in this figure. This is the probability of finding turbulence at a given space–time point. The velocity $\langle u' \rangle$ and the pressure $\langle p'_{\mathrm{R}} \rangle$ increase sharply as the turbulent front is approached, attaining maxima of the order of their r.m.s. values approximately at the time when the turbulent front is detected. This feature can be interpreted by an inrush of outer
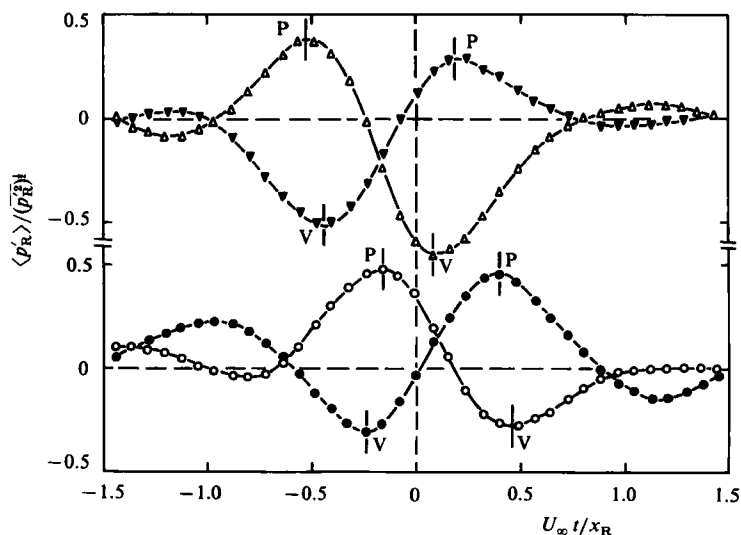
FIGURE 12. Phase-averaged surface-pressure fluctuation at the reattachment point; time t is synchronized with zeros A (open symbols) and zeros B (solid symbols) of the surface velocity measured at (a) $(x-x_R)/x_R = 0.05$ ($\triangle$, $\blacktriangledown$) and (b) -0.05 ($\bigcirc$, $\bullet$): P and V imply peaks and valleys, respectively, of $\langle p'_R \rangle$.

irrotational fluid with high total pressure towards the wall. This inrush produces positive spikes in the surface-pressure waveforms, yielding a positive skewness of the pressure fluctuation in the reattaching zone (KS).

3.3. *Reverse-flow unsteadiness in the reattaching zone associated with large-scale vortices*

The unsteady flow in the reattaching zone is dominated by two agents: the motion of the large-scale vortices; and the low-frequency unsteadiness. In this section we will discuss the former, the latter being the subject of §3.4.

An aspect of the unsteadiness can be demonstrated by the motion of reverse-flow regions. A reverse-flow region is defined in this paper as a region where the instantaneous longitudinal velocity near the surface is negative; the velocity at the height 0.5 mm ($\simeq 0.005x_R$) was chosen rather arbitrarily. This velocity was short-time averaged with an averaging time 0.8 ms which is approximately one-tenth of the vortex-shedding period. In what follows, the short-time averaged velocity will be called the 'surface velocity' u_s for convenience.

A boundary between a reverse-flow region and a forward-flow region is characterized by either $u_s = 0$, $\partial u_s / \partial t < 0$ or $u_s = 0$, $\partial u_s / \partial t > 0$ when we measure u_s as a function of time at a given position x; the former will be denoted by zero A and the latter by zero B. If we could measure the spatial distribution of u_s at a given time, zeros A and B would be identified as positions $u_s = 0$, $\partial u_s / \partial x > 0$ and $u_s = 0$, $\partial u_s / \partial x < 0$, respectively. We feel that positions of zeros A and B are not far from positions where the instantaneous shear stress at the surface is zero.

At a given longitudinal position in the reattaching zone, the surface velocity was sampled to find zeros A and B. The time at which zero A or B was detected was then employed as the synchronization time to phase-average the surface-pressure fluctuation p'_R at the reattachment point. A few examples of the phase-averaged pressure $\langle p'_R \rangle$ are shown in figure 12 for two positions $x/x_R = 0.95$ and 1.05. A peak
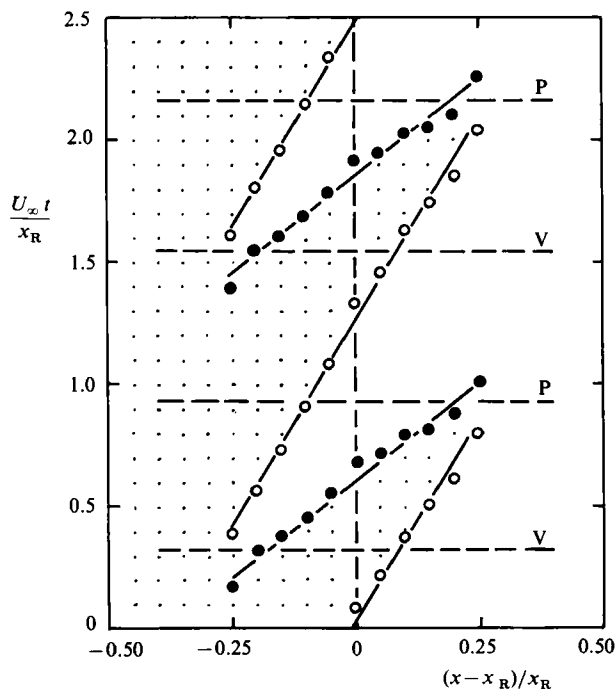
FIGURE 13. Motion of zeros A and B of the surface velocity in the space–time $(x-x_R, t)$ domain: broken horizontal lines denoted by P and V indicate the time at which the phase-averaged pressure fluctuation $\langle p'_R \rangle$ attains a peak and a valley, respectively; $\bigcirc$, A; $\bullet$, B; shaded area is reverse-flow region; origin of time t is arbitrary.

P and a valley V are observed in each curve of figure 12. It is reasonable to assume that a peak P or a valley V shows a particular phase of the motion of the large-scale vortices in the reattaching zone because the motion has strong correlation with p'_R, as demonstrated in §3.1. Accordingly, we can measure the time when zero A or B appears from the time of P or V, which will be denoted by t_P or t_V, respectively. Figure 12 shows that the difference in time $|t_P - t_V|$ has a fairly constant value of $0.62 x_R/U_\infty$ in each curve of $\langle p'_R \rangle$. This was also the case for other positions x in the reattaching zone. The reciprocal of twice the time difference can be interpreted as the frequency of shedding of the large-scale vortices, amounting to $0.81 U_\infty/x_R$. This is 25 % larger than the actual vortex-shedding frequency $0.65 U_\infty/x_R$. The difference between the two frequencies is possibly caused by the dispersion of the large-scale vortices in strength and position.

The motion of zeros A and B in the space–time $(x-x_R, t)$ domain is shown in figure 13. We observe one reverse-flow region or two in the reattaching zone, the number of the reverse-flow regions depending on time. Zero B moves with the speed of about $0.7 U_\infty$, which is much faster than the speed $0.3 U_\infty$ of zero A; the average speed $0.5 U_\infty$ is equal to the convection velocity of the large-scale vortices. It is interesting to note that peak P appears when zero B has caught up with zero A near the downstream end of the reattaching zone $(x/x_R \simeq 1.2$, see KS), that is, when the downstream reverse-flow region vanishes. On the other hand, valley V occurs when a forward-flow region emerges near the upstream end of the reattaching zone $(x/x_R \simeq 0.8)$.
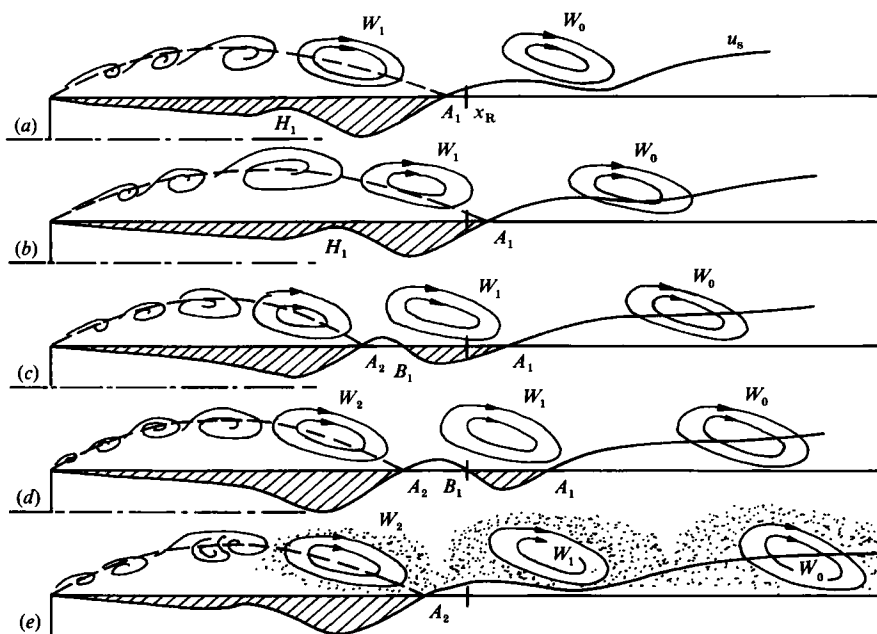
FIGURE 14. Schematic representation of motion of zeros A and B and large-scale vortices: hatched areas are reverse-flow regions; dotted area shows poorly correlated region around vortices; broken lines show centre of separated shear layer.

Figure 13 suggests a relation between the motion of zeros in the surface velocity and that of the large-scale vortices such as sketched in figure 14 for one period of the vortex shedding. At phase (a) a large vortex W_0 has been shed and the next vortex W_1 is now approaching to the upstream end of the reattaching zone. There is no reverse flow beneath the vortex W_0 partly owing to its acceleration in, and downstream of, the reattaching zone (see KS) and partly owing to a decay of its strength caused by turbulent diffusion of vorticity. There is only one zero A_1 in the surface velocity.

The vortex W_1 and the zero A_1 have moved a little downstream at phase (b); a maximum H_1 of the surface-velocity profile becomes higher at this phase than at phase (a). The maximum H_1 becomes even higher at phase (c) to give rise to new zeros A_2 and B_1, producing a forward-flow region between the two zeros. A reverse-flow region $A_1 B_1$ is now beneath the vortex W_1. In view of figure 13 the surface-pressure fluctuation p'_R at the reattachment point attains a valley V approximately at this phase (c). The zero B_1 moves much faster than the zeros A_1 and A_2; at phase (d) this difference in the speed of the zeros has extended the forward-flow region $A_2 B_1$ and contracted the reverse-flow region $A_1 B_1$. Finally, just before phase (e), the zero B_1 has caught up with the zero A_1, so that the reverse-flow region disappears at phase (e). Then the next cycle of the vortex shedding begins. The feature mentioned above is consistent with the result of a discrete-vortex simulation by Arie, Kiya & Sasaki (1983).

3.4. *Properties of low-frequency unsteadiness*

In this section properties of the low-frequency unsteadiness will be presented and discussed in more detail than in previous studies (Hillier & Cherry 1981; Eaton & Johnston 1982; KS). A recent paper of Cherry *et al.* (1984) demonstrates some new
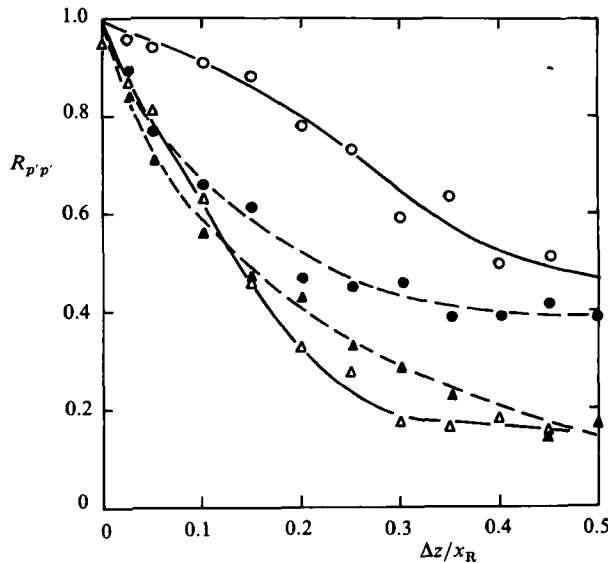
FIGURE 15. Spanwise correlation coefficients of surface-pressure fluctuations along lines $x/x_R = 0.2$ (open symbols $\bigcirc$, $\triangle$) and 1.0 (solid symbols $\bullet$, $\blacktriangle$): one pressure transducer was fixed at the mid span and the other was traversed in the spanwise direction; $\bigcirc$, $\bullet$, low-pass filtered component; $\triangle$, $\blacktriangle$, high-pass filtered component; the cut-off frequency was 50 Hz ($\simeq 0.25 U_\infty/x_R$).

aspects of this unsteadiness by combining visualized-flow patterns with waveforms of the surface-pressure fluctuations.

The low-frequency unsteadiness is of large scale in the sense that it is felt everywhere in the separation bubble. Its spanwise extent is demonstrated in figure 15 in terms of the spanwise correlation of the surface-pressure fluctuations shortly downstream of the separation line and along the reattachment line. Here the correlation is presented separately for low-pass filtered and high-pass filtered pressure fluctuations, the cut-off frequency being the uppermost frequency of the low-frequency unsteadiness ($= 0.25 U_\infty/x_R$). The low-pass filtered components are mainly contributed by the low-frequency unsteadiness and the high-pass filtered components by the motion of the large-scale vortices in the reattaching zone.

The low-frequency correlation near the separation line ($x/x_R = 0.2$) is seen to decay much slower than the high-frequency correlation, so that the low-frequency unsteadiness has a larger spanwise lengthscale. On the other hand, the low-frequency correlation decays much faster on the reattachment line than on the upstream line. This is because in the reattaching zone the low-frequency pressure fluctuation was of much lower level than the high-frequency fluctuation. Moreover, the mean square value $\overline{p_1'^2}$ (not presented here) was approximately half that of the overall fluctuation $\overline{p'^2}$ ($= \overline{p_1'^2} + \overline{p_h'^2}$) in the forward part $x/x_R < 0.4$ of the bubble; at $x/x_R = 0.4$, $\overline{p_1'^2}$ fell sharply to $0.13\overline{p'^2}$ to remain constant up to the reattachment line.

The results mentioned above suggest that the low-frequency unsteadiness is most strongly felt in the forward part. It is reasonable to assume that peaks and valleys of the low-frequency pressure fluctuation at a position in the forward part correspond to a particular phase of this unsteadiness. A position $x/x_R = 0.2$ was rather arbitrarily chosen as the point of detecting the pressure fluctuation, which is denoted by p_{21}'.
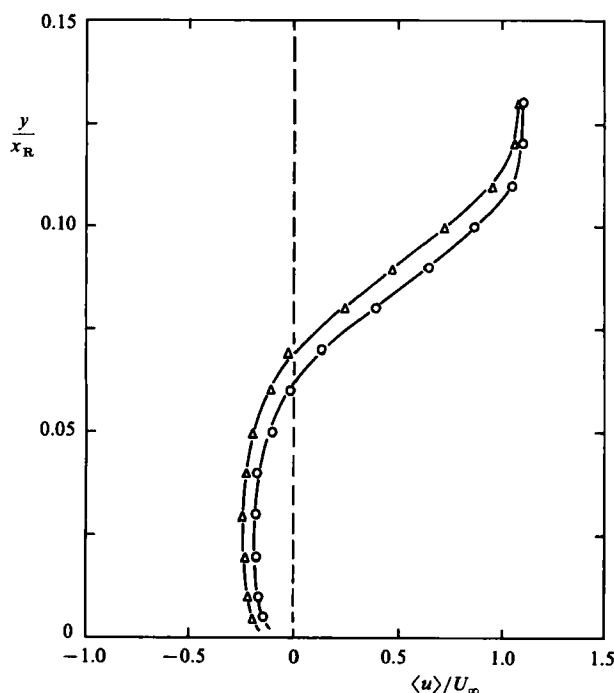
FIGURE 16. Profile of longitudinal velocity component conditionally averaged at the time when low-pass filtered surface-pressure fluctuation attains peaks and valleys: velocity and pressure were measured at $x/x_R = 0.2$; $\triangle$, peaks; $\bigcirc$, valleys; the cut-off frequency was 50 Hz ($\simeq 0.25 U_\infty/x_R$). The threshold levels for the peaks and the valleys were $1.0(\overline{p_{21}^2})^{\frac{1}{2}}$ and $-1.0(\overline{p_{21}^2})^{\frac{1}{2}}$, the detection frequencies being 19 Hz and 17 Hz, respectively.

The longitudinal velocity u at several points above this position at the mid span was conditionally averaged at the times when p_{21}' attained peaks and valleys.

The result is presented in figure 16, which clearly establishes the existence of the flapping motion of the shear layer. The centre of the shear layer is seen to shift towards the surface at the valleys and away from the surface at the peaks. This is consistent with the conjecture of KS. The amplitude of the flapping motion is rather small, being approximately $0.005x_R$.

The fact that the low-frequency unsteadiness is felt throughout the bubble is demonstrated in figure 17 in terms of the cross correlation of the low-pass filtered velocity and pressure fluctuations $R_{u_1' p_1'}$; the velocity u_1' was detected at a fixed position $(x, y)/x_R = (0.2, 0.15)$ (just outside the time-mean edge y_δ of the shear layer) and the pressure fluctuation p_1' at various positions along the mid span.

Figure 17 shows that the correlation is positive in a region $0.6 \lesssim x/x_R \lesssim 1.3$ centred around the reattachment line, becoming negative on each side of it. This feature can be interpreted in the following way. We assume that the pressure fluctuation p_1' is produced by an oscillatory motion of the time-mean pressure profile in the longitudinal direction. The pressure profile (see figure 7 of Kiya, Sasaki & Arie 1982) has a broad maximum at $x/x_R \simeq 0.4$ and a broad minimum at $x/x_R \simeq 1.4$. Accordingly, if the pressure profile shifts upstream p_1' becomes positive in the region $0.4 \lesssim x/x_R \lesssim 1.4$ and negative on both sides of it; p_1' is approximately zero at $x/x_R = 0.4$ and 1.4, which are not very far from the positions where the cross
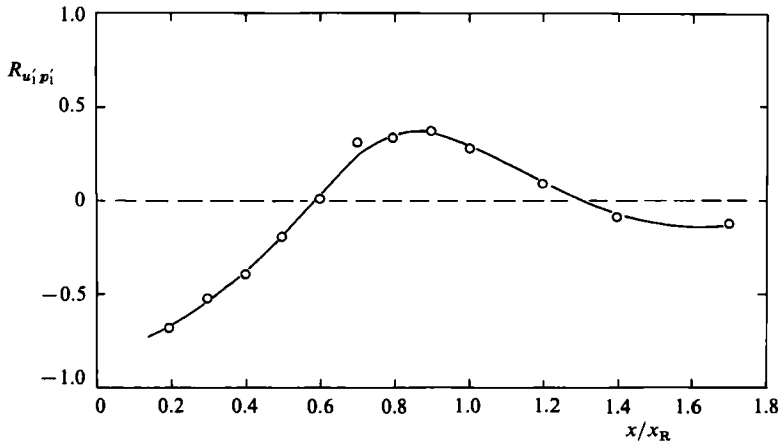
FIGURE 17. Cross correlation of low-pass filtered components u_1' and p_1' of longitudinal-velocity and surface-pressure fluctuations, respectively: the cut-off frequency was 50 Hz ($\simeq 0.25 U_\infty/x_R$); velocity was measured at a fixed position $(x, y)/x_R = (0.2, 0.15)$ which is immediately outside edge of shear layer y_δ; the pressure transducer was traversed along the mid span.

correlation is zero. The positive cross correlation in the region $0.6 \lesssim x/x_R \lesssim 1.3$ implies that p_1' is generally positive at an instant when u_1' is positive. Accordingly, since positive u_1' occurs when the shear layer shifts towards the surface, the downward motion of the shear layer is accompanied by the upstream motion of the time-mean pressure profile near the reattachment line, viz a shrinkage of the separation bubble. By the same reasoning the upward shift of the shear layer is accompanied by an enlargement of the bubble.

The above consideration suggests that the velocity and pressure fluctuations associated with the low-frequency unsteadiness can be approximated by a standing wave whose frequency is equal to the central frequency of the unsteadiness. This will be used in §4 to construct a mathematical model of the surface-velocity fluctuation in the reattaching zone.

Some properties of the enlargement and shrinkage of the separation bubble can be obtained by means of the low-pass filtered surface velocity u_{s1}. We interpret a position where u_{s1} in the reattaching zone attains zero as an instantaneous reattachment position. Two kinds of zeros can be distinguished in the waveforms of u_{s1} measured at a fixed position; one which will be denoted by A_1 is defined by $u_{s1} = 0$ and $\partial u_{s1}/\partial t < 0$ and the other which will be denoted by B_1 by $u_{s1} = 0$ and $\partial u_{s1}/\partial t > 0$. The motions of zeros A_1 and B_1 were obtained in the following way. At a fixed position x in the reattaching zone, zeros A_1 were searched for and the time at which A_1 was detected was then employed as the synchronization time against which the low-pass filtered pressure fluctuation at the reattachment point p_{R1}' was phase-averaged. The same procedure was also followed for zeros B_1. An example of the phase-averaged pressure $\langle p_{R1}' \rangle$ is shown in figure 18 in which zeros A_1 and B_1 were detected at a position $(x-x_R)/x_R = -0.01$. The pressure $\langle p_{R1}' \rangle$ is seen to attain a peak P_1 and a valley V_1 for both A_1 and B_1. The time interval between P_1 and V_1 was found to have a fairly constant value $40x_R/U_\infty$ for both zeros obtained at various positions x in the reattaching zone. The reciprocal of twice this time interval coincides well with the central frequency $0.12 U_\infty/x_R$ of the low-frequency unsteadiness.

It is reasonable to assume that a peak or a valley of $\langle p_{R1}' \rangle$ corresponds to a
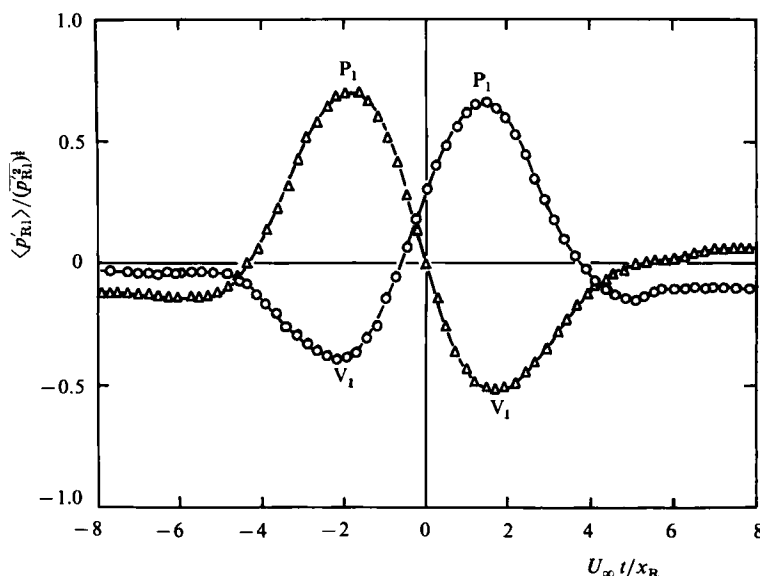
FIGURE 18. Low-pass filtered surface-pressure fluctuation $\langle p'_{\mathrm{Rl}} \rangle$ (at the reattachment point) conditionally averaged with respect to the time when zeros A_1 and B_1 of low-pass filtered surface velocity were detected at $(x - x_{\mathrm{R}})/x_{\mathrm{R}} = -0.01$: the cut-off frequency was 50 Hz ($\simeq 0.25 U_\infty / x_{\mathrm{R}}$); $\triangle$, A_1; $\bigcirc$, B_1; P_1 and V_1 are peaks and valleys of $\langle p'_{\mathrm{Rl}} \rangle$, respectively.

particular phase of the enlargement and shrinkage of the separation bubble. Accordingly the times when zeros A_1 and B_1 appear at a given position x were measured relative to the times when the peaks P_1 or the valleys V_1 were recorded. By repeating the same measurement at various longitudinal positions, we obtained the motions of zeros A_1 and B_1 in the space–time (x, t) domain. The result is presented in figure 19. Zeros A_1 move upstream while zeros B_1 move downstream; the speed is much greater for B_1 than for A_1. An estimation showed that the speeds of A_1 and B_1 are approximately $0.1 U_\infty$ and $0.2 U_\infty$, respectively, at a point (x, t) midway between P_1 and V_1. In other words, the shrinkage of the separation bubble is much swifter than the enlargement. Eaton & Johnston (1980) suggest such a difference in the speed of the shrinkage and enlargement but they are unable to find the difference in their own experiment.

The low-frequency unsteadiness is expected to produce some changes in the properties of the large-scale vortices. In order to find out whether this is true, the power spectrum of the pressure fluctuation at the reattachment point was separately obtained in the shrunk and enlarged states. On average six vortices are shed during one period of the low-frequency unsteadiness, viz three vortices during the shrunk state and another three vortices during the enlarged state, because the vortex-shedding frequency is approximately six times the central frequency of the low-frequency unsteadiness. We detected the time at which the low-pass filtered pressure p'_{Rl} attained a peak P_1 at which the separation bubble is in the shrunk state. The original pressure fluctuation p'_{R} was then sampled during about a half of the period of the low-frequency unsteadiness (centred around the time when the peak was found). The sampled pressure fluctuation was Fourier-analysed to obtain the spectrum $E_{p'_{\mathrm{R}}}$. By repeating the same procedure for many peaks P_1 and adding the resulting spectra, we obtained the conditionally averaged spectrum $\langle E_{p'_{\mathrm{R}}} \rangle$. The corresponding spectrum was also obtained for valleys of V_1 of p'_{Rl}.
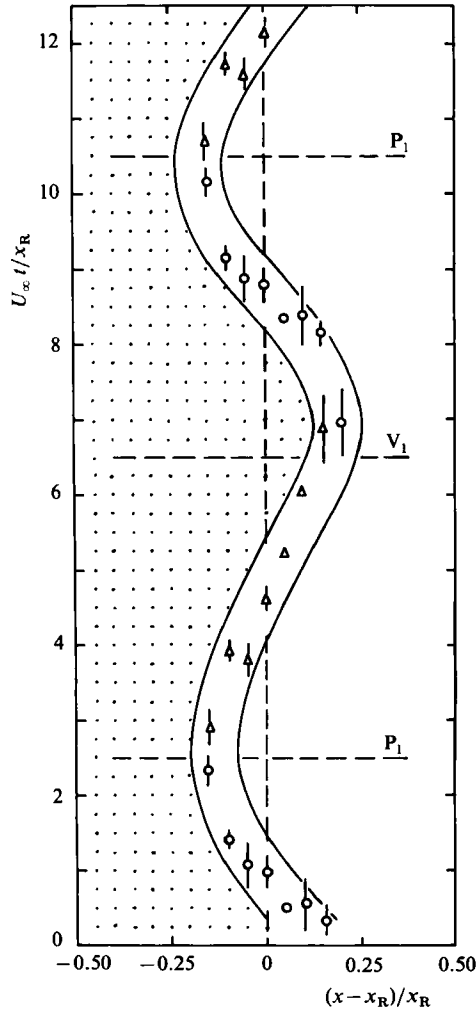
FIGURE 19. Motion of zeros A_1 and B_1 of low-pass filtered surface velocity in the space–time $(x - x_R, t)$ domain: $\triangle$, A_1; $\bigcirc$, B_1; flags added to symbols and solid lines represent the range of experimental uncertainty; horizontal broken lines denoted by P_1 and V_1 indicate the time at which the phase-averaged pressure $\langle p'_{R1} \rangle$ attains peaks and valleys, respectively; the origin of time t is arbitrary; the shaded area represents a reverse-flow region.

The result is shown in figure 20 where $f\langle E_{p'_R} \rangle$, f being the frequency, is plotted against $f x_R / U_\infty$ on a semilogarithmic scale. The spectra have a peak at a frequency $0.6 U_\infty / x_R$, which is the shedding frequency of the large-scale vortices. The spectrum peak is clearly much higher for the peaks P_1 than for the valleys V_1. This feature can be interpreted in the following way. In the reattaching zone, the large-scale vortices are in contact with the surface, so that the average distance between the vortex centre and the surface can be assumed to be fairly constant. On this assumption, the stronger the vortices, the greater is the pressure fluctuation associated with the motion of the large-scale vortices. The height of the spectrum peak is thus a measure of the strength of the vortices in the reattaching zone. Figure 20 shows that the vortices shed during the shrunk state are stronger than those shed during the enlarged state. In other
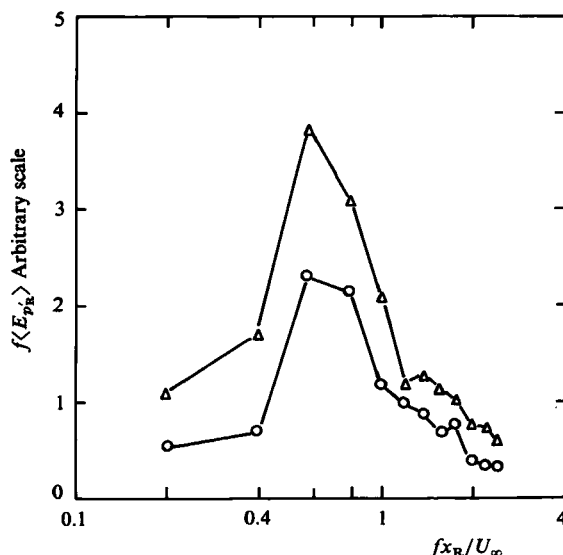
FIGURE 20. Pressure spectra for enlarged and shrunk states of separation bubble due to low-frequency unsteadiness: pressure p'_i was detected at the reattachment point; $\triangle$, shrunk state; $\bigcirc$, enlarged state. The enlarged and shrunk states were defined by valleys V_1 and peaks P_1 of p'_R. The threshold levels for the peaks and the valleys are $1.8(\overline{p'^2_{R1}})^{\frac{1}{2}}$ and $-1.8(\overline{p'^2_{R1}})^{\frac{1}{2}}$, the detection frequencies being 14 Hz and 11 Hz, respectively.

words, the strength of the shed vortices is possibly dependent on the phase of the low-frequency unsteadiness.

The exact origin of the low-frequency unsteadiness is not understood yet. Eaton & Johnston (1982) suggest that this is probably caused by an instantaneous imbalance between the entrainment (by the shear layer) from the recirculating zone and reinjection of fluid near the reattachment line. If we assume that the bubble length is determined by the balance between the entrainment rate and the reinjection rate, such an instantaneous imbalance could cause the enlargement or shrinkage of the bubble. In this regard Eaton & Johnston (1982) envision the motion associated with the low-frequency unsteadiness being roughly two-dimensional and conjecture as follows. 'An *unusual* event may cause a short-term breakdown of the spanwise vortices in the shear layer. The entrainment rate would be temporarily decreased, while the reinjection rate remained constant. This would cause an increase in the volume of recirculating fluid, thus moving the shear layer away from the wall and increasing the short-time averaged reattachment length.' We feel that this conjecture is reasonable and further infer that the short-term breakdown of the spanwise vortices results in a decrease in the spanwise coherence of the large-scale vortices in the reattaching zone. This decrease in the spanwise coherence can probably produce a decrease in the strength of the large-scale vortices and thus a decrease in the peak height of the pressure spectra. By the same reasoning, the high peak of the pressure spectra for the peaks P_1 is associated with an increase in the strength of the large-scale vortices in the reattaching zone. This increase is probably brought about by a recovered spanwise coherence of the shear-layer vortices in the forward part of the bubble. A greater spanwise coherence produces a greater entrainment of fluid from the recirculating zone; this enhanced entrainment thus results in a decrease in the instantaneous reattachment length.

We believe that the fairly constant periodicity of the low-frequency unsteadiness indicates a feedback of disturbances from the reattaching zone to the shear layer near the separation line (Rockwell 1983), although Eaton & Johnston (1982) assume an unusual event as a cause of the short-term breakdown of the spanwise vortices. The disturbances are possibly created by the change of the vortex strength in the reattaching zone, propagating upstream as pressure waves.

It is suggested in KS that the low-frequency unsteadiness is accompanied by the shedding of an extremely large vortex. We now have a different opinion about this; the shedding of such vortices does occur but this is a relatively rare event in view of the result shown in figures 19 and 20. The low-frequency unsteadiness is possibly an event difficult to observe by conventional flow-visualization techniques. It is possible that this unsteadiness is different from that observed by Cherry *et al.* (1984) through smoke flow visualizations.

4. A model for the unsteadiness in the reattaching zone

As mentioned in §3.3, the unsteady flow in the reattaching zone is mainly produced by two agents; one is the unsteadiness due to the motion of the large-scale vortices, while the other is that due to the low-frequency unsteadiness. In this section we present a model for the surface-velocity fluctuation in the reattaching zone to demonstrate the role of the two agents in determining the statistical properties of the unsteady flow such as the reverse-flow intermittency, the frequency of switching of the local-flow direction, etc.

The surface-velocity fluctuation due to the motion of the large-scale vortices is approximated by a sinusoidal travelling wave with the phase velocity U_c, the frequency f_h and the amplitude U_h. On the other hand, the velocity fluctuation due to the low-frequency unsteadiness is approximated by a sinusoidal standing wave with the frequency f_l and the amplitude U_l. Accordingly, this model does not include the difference in the speed of the enlargement and shrinkage of the bubble. Under the above assumptions, the instantaneous surface velocity u_s can be written as

$$u_s = U_s + u'_{sh} + u'_{sl},$$

where U_s is the time-mean component and u'_{sh} and u'_{sl} are the fluctuating components given by

$$u'_{sh} = U_h \sin\left\{2\pi f_h\left(t - \frac{x^*}{U_c}\right) + \psi_h\right\},$$

and

$$u'_{sl} = U_l \sin\left(2\pi f_l t + \psi_l\right).$$

Here t is the time, x^* is $x - x_R$ and ψ_h and ψ_l denote phase angles. Values of the parameters included in the above equations will be determined from the experimental results.

As shown in figure 10 of KS, U_s near the reattachment line is well represented by

$$U_s = (dU_s/dx^*)_{x^*=0} x^* \simeq 0.08(U_\infty/H) x^*.$$

The amplitudes U_h and U_l are taken as $\sqrt{2}$ times the r.m.s. value (not shown here) of the low- and high-pass filtered components, respectively, of the surface-velocity fluctuation at the reattachment point; the result is

$$U_h \simeq 0.18 U_\infty \quad \text{and} \quad U_l \simeq 0.10 U_\infty.$$

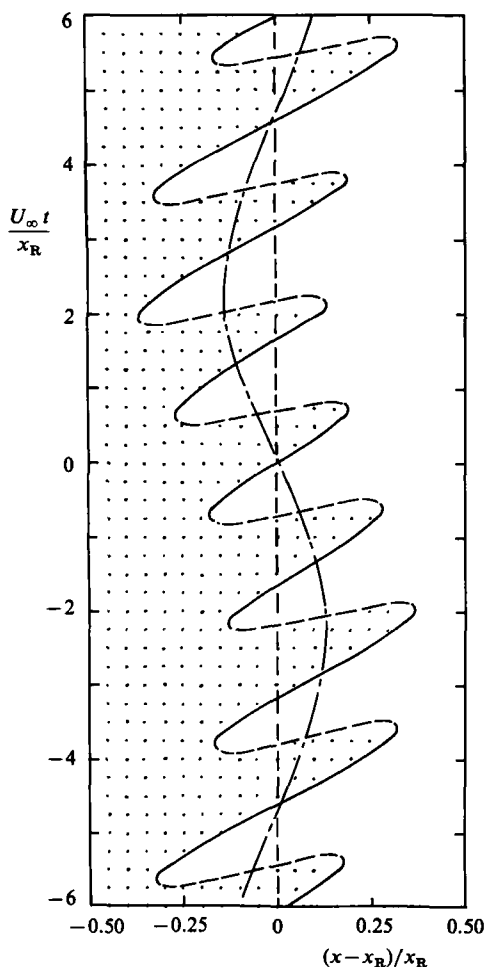The phase velocity U_c is the convection velocity of the large-scale vortices which is

FIGURE 21. Calculated motion of zero-velocity points A and B in the space–time $(x-x_R, t)$ domain: ——, A; – – –, B; – · –, component due to low-frequency unsteadiness; origin of time t is arbitrary; the shaded area is a reverse-flow region.

on average $0.5U_\infty$ in the reattaching zone (see KS). Finally, the frequencies f_h and f_l are taken as $0.65U_\infty/x_R$ and $\frac{1}{6}f_h$ respectively.

With the values of the parameters thus determined, we can obtain an ensemble of the points (x^*, t) satisfying the condition $u_s = 0$ for a given combination of the phase angles. The result for $\psi_h = 0$ and $\psi_l = \pi$ is shown in figure 21. A large excursion of the zero-velocity points in the longitudinal direction is observed; the maximum excursion amounts to approximately $0.3x_R$ on each side of the reattachment point.

Figure 21 also demonstrates that the low-frequency unsteadiness produces a temporally non-uniform appearance of the zero-velocity points. Taking, for example, a position $x^*/x_R = -0.2$, flow reversals occur in bursts during certain time intervals $(U_\infty t/x_R = 0.5$–4.0, for example); these time intervals are separated by times when the flow direction is steady. On the other hand, when a burst of flow reversals is occurring at this position, no reversals occur at the opposite position $x^*/x_R = +0.2$. This feature is observed experimentally by Eaton & Johnston (1982) behind a backward-facing step, and also in this experiment. It should be noted that Eaton &
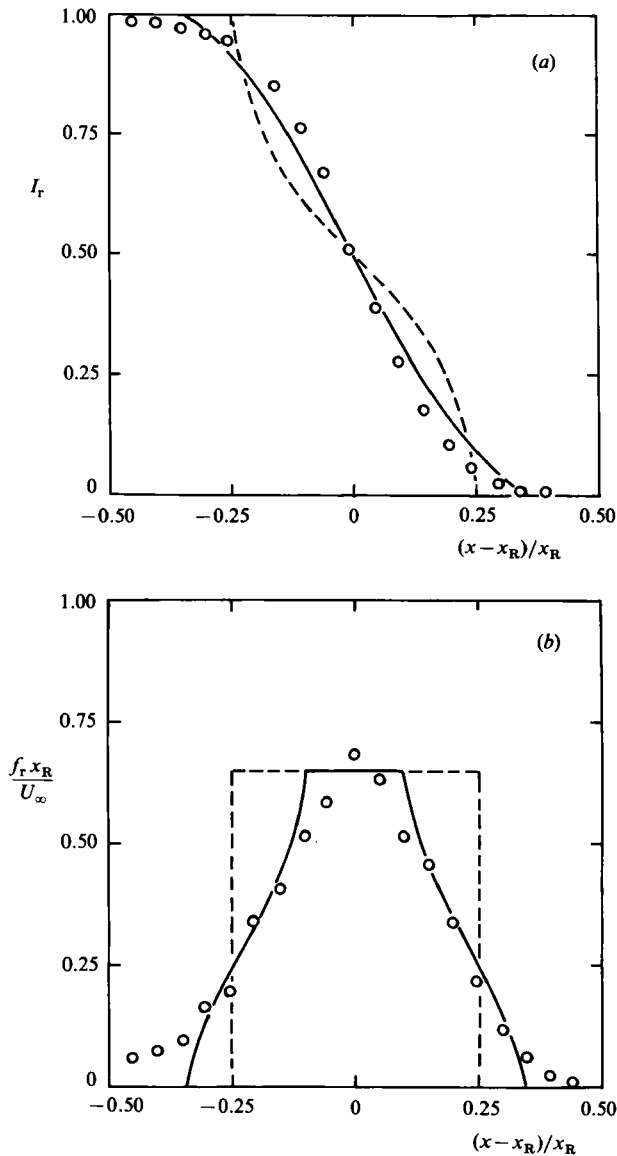
FIGURE 22. Comparison of calculated and measured reverse-flow properties: (a) reverse-flow intermittency; (b) frequency of switching of local-flow direction; ———, calculation including both u'_{sh} and u'_{sl}; — — —, calculation including u'_{sh} only; ○, measurement.

Johnston (1982) correctly suggest the burst-like occurrence of the flow reversals to be caused by the low-frequency unsteadiness. Figure 21 may give an impression that the whole process is more regular and periodic than is apparent from smoke flow visualizations (Cherry *et al.* 1984). The phase angles ψ_h and ψ_l are allowed to change at random, so that the suggested process is not so regular as imagined from figure 21.

Another aspect of the model will now be discussed. The reverse-flow intermittency I_r, the frequency of flow reversals f_r, etc. can be calculated at a given longitudinal position x^* by means of the trajectories of the zero-velocity points (such as are shown

in figure 21) constructed for various combinations of the phase angles. The prediction of the model is compared with the present experiment in figure 22. A fairly good agreement is obtained. If I_r and f_r are calculated from u'_{sh} only (viz the surface-velocity fluctuation due to the motion of the large-scale vortices), their distributions are very different from the experimental result, as shown in figure 22. In order to have reasonable agreement, we must include the effect of the low-frequency unsteadiness. This clearly shows that the low-frequency unsteadiness plays a vital role in determining the statistical properties of the unsteady flow in the reattaching zone.

5. Further discussion and conclusions

This paper has described the properties of the large-scale vortices and those of the unsteady reverse flow in the reattaching zone of a turbulent separation bubble formed at the leading edge of a blunt flat plate. Some of the results are generally applicable to nominally two-dimensional separation bubbles at salient edges.

The conditionally averaged velocity vectors and the contour lines of the high-frequency turbulent energy in the space–time domains (y, t) and (z, t) yield a three-dimensional feature of the large-scale vortices in the reattaching zone. These large-scale vortices originate from a successive amalgamation of vortices formed in the separated shear layer owing to the Kelvin–Helmholtz instability.

The large-scale vortices in the reattaching zone have a hairpin shape with its ends lying probably in the (x, y)-plane, each end rotating in opposite directions so as to lift up fluid between them (see figure 8). The spanwise distance between the ends is approximately $0.6x_R$. This is almost the same as the longitudinal spacing between two consecutive large-scale vortices in the reattaching zone. This is noteworthy because it is known that the spanwise distance between the streamwise vortices in the transition region of an initially laminar mixing layer is approximately equal to the Kelvin–Helmholtz spacing (Roshko 1981). The streamwise vortices are probably produced by a centrifugal instability at the trough between two consecutive spanwise vortices (Taneda 1983), and thus adjust themselves to the spanwise vortices whose lengthscale increases with increasing longitudinal distance from the beginning of the shear layer. Roshko (1981) states that possibly the streamwise vortices are generated locally, forming streamwise elongated loops, which line up by mutual interaction to produce a pattern of extended streamwise streaks, and changing scale only when the primary (i.e. spanwise) scale has developed to a sufficiently large value. The hairpin vortices found in the reattaching zone are probably produced by the same mechanism. This immediately leads to the conjecture that the hairpin vortices are universal to nominally two-dimensional separation bubbles formed at the salient edges.

The velocity-vector fields shown in figures 6 and 7 suggest that two consecutive large-scale vortices are arranged in such a way that their centres are at the same spanwise location. It is not clear, however, whether or not this arrangement is particular to the present experiment. The somewhat small aspect ratio of the plate tested, which is two in terms of the bubble length, is possibly responsible for such arrangement.

The surface-pressure fluctuation in the reattaching zone was extensively used in this study as a conditioning signal to obtain the space–time distributions of the fluctuating velocity vectors in the large-scale vortices. This approach was successful because the motion of the large-scale vortices produces pressure fluctuations with a sufficiently large amplitude in the reattaching zone.

We are well aware that pressure fluctuations are not a local quantity because the

pressure fluctuation at a given point is in principle influenced by velocity fluctuations in the whole region of flow. Contributions from distant regions, however, fall off rapidly with increasing distance from the point under consideration, so that the near-field contribution is the greatest contribution. It is assumed in this study that the greatest contribution comes from the large-scale vortices in the high-frequency range and from the low-frequency unsteadiness in the low-frequency range. It is, however, possible that a strong local event produces a sufficiently high amplitude of the surface-pressure fluctuation having no direct connection either with the large-scale vortices or with the low-frequency unsteadiness. Such strong local events, if any, are probably so rare that their effects on the conditionally averaged velocity-vector fields (figures 4–7) are insignificant. The fact that these vector fields have a meaningful pattern is a piece of evidence that this conjecture is correct; the vector fields have been smeared by the local events to a certain extent. The smearing effect can be reduced by employing pressure fluctuations at several suitably arranged positions as the conditioning signals. This would be a good subject for future work.

The existence of the large-scale low-frequency unsteadiness is well established in this study. The low-frequency unsteadiness has relatively good two-dimensionality in the forward part of the separation bubble where the shear layer experiences a flapping motion. The unsteadiness is probably an inherent feature of nominally two-dimensional separation bubbles formed at the salient edges, because this is also observed behind a backward-facing step (Eaton & Johnston 1982) and in the leading-edge separation bubble with high free-stream turbulence (Cherry, Hillier & Latour 1983).

We hope that the present paper has demonstrated several new aspects of the flow in the reattaching zone of nominally two-dimensional separation bubbles. Finally, some of the future problems to be tackled are (i) clarifying the feedback mechanism to sustain the low-frequency unsteadiness, (ii) obtaining more detailed information about the three-dimensional structure of the large-scale vortices by multiple-point measurements, (iii) reproducing the turbulence properties in the reattaching zone by suitable modelling of the large-scale vortices and the low-frequency unsteadiness, (iv) clarifying the mechanism responsible for high heat- and mass-transfer rates in the reattaching zone and (v) manipulating the flow in the reattaching zone, for example by the treatment of the separation edges.

REFERENCES

ARIE, M., KIYA, M. & SASAKI, K. 1983 Leading-edge separation bubble simulated by a discrete-vortex model. *Trans. JSME* **B49**, 923–930 (in Japanese).

BRADSHAW, P. & WONG, F. Y. F. 1972 The reattachment and relaxation of a turbulent shear layer. *J. Fluid Mech.* **52**, 113–135.

CHANDRSUDA, C. & BRADSHAW, P. 1981 Turbulence structure of a reattaching shear layer. *J. Fluid Mech.* **110**, 171–194.

CHERRY, N. J., HILLIER, R. & LATOUR, M. E. M. P. 1983 The unsteady structure of two-dimensional separated-and-attaching flows. *J. Wind Engng & Ind. Aerodyn.* **11**, 95–105.

CHERRY, N. J., HILLIER, R. & LATOUR, M. E. M. P. 1984 Unsteady measurements in a separated and reattaching flow. *J. Fluid Mech.* **144**, 13–46.

EATON, J. K. & JOHNSTON, J. P. 1980 Turbulent flow reattachment: an experimental study of the flow and structure behind a backward-facing step. *Rep* MD-39, *Thermosciences Division, Department of Mechanical Engineering, Stanford University, Stanford, California.*

EATON, J. K. & JOHNSTON, J. P. 1981 A review on subsonic turbulent flow reattachment. *AIAA J.* **19**, 1093–1100.

EATON, J. K. & JOHNSTON, J. P. 1982 Low frequency unsteadiness of a reattaching turbulent shear layer. In *Turbulent Shear Flows 3* (ed. L. J. S. Bradbury, F. Durst, B. E. Launder, F. W. Schmidt & J. H. Whitelaw), pp. 162–170. Springer.

HILLIER, R. & CHERRY, N. J. 1981 Pressure fluctuations under a turbulent shear layer. In *Proc. 3rd Turbulent Shear Flow Symp., Davis, California, 9–11 September*, pp. 16.23–16.28.

KIYA, M. & SASAKI, K. 1983 Structure of a turbulent separation bubble. *J. Fluid Mech.* **137**, 83–113.

KIYA, M., SASAKI, K. & ARIE, M. 1982 Discrete-vortex simulation of a turbulent separation bubble. *J. Fluid Mech.* **120**, 219–244.

OTA, T. & KON, N. 1974 Heat transfer in the separated and reattached flow on a blunt flat plate. *Trans. ASME* C: *J. Heat Transfer* **96**, 459–462.

ROCKWELL, D. 1983 Oscillations of impinging shear layers. *AIAA J.* **21**, 645–664.

ROSHKO, A. 1981 The plane mixing layer flow visualization results and three-dimensional effects. Lecture Notes in Physics **136**, pp. 208–217. Springer.

TANEDA, S. 1983 Visual observation on the amplification of artificial disturbances in turbulent shear flows. *Phys. Fluids* **26**, 2801–2806.

WOOD, D. H. & BRADSHAW, P. 1982 A turbulent mixing layer constrained by a solid surface. Part 1. Measurements before reaching the surface. *J. Fluid Mech.* **122**, 57–89.